

Quasi-Reflectionless Filters Using Simple Coupled Line and T-Shaped Microstrip Structures

Kai-Da Xu¹, Senior Member, IEEE, Sen Lu², Ying-Jiang Guo³, Member, IEEE,
and Qiang Chen⁴, Senior Member, IEEE

Abstract—In this paper, two simple structures, i.e., coupled line and T-shaped microstrip structures, are used to construct four types of quasi-reflectionless (QR) filters, including single- and two-port QR bandpass filters (BPFs) and bandstop filters (BSFs). First, the characteristics of the coupled line and T-shaped microstrip structures are analyzed in details using each two electrical parameters. Then, the single-port QR BPF and BSF are designed using duplexer architectures formed by these two simple structures. Subsequently, the two-port QR BPF and BSF are constructed through loading an additional absorption channel near the output port based on the architectures of single-port QR filters. The relations between the fractional bandwidth (FBW) of each type of QR filters and 3-dB FBWs of the two simple structures are provided, which give a guidance of the QR filter design with desired specifications. Moreover, a brief design procedure for the proposed QR filters is summarized. Finally, to validate the feasibility of the proposed approach, two proof-of-concept microstrip prototypes of the two-port QR filters are fabricated, whose simulations and measurements agree well with each other. This work will facilitate the design of QR filters with different desired specifications and simplify their design procedures.

Index Terms—Bandpass filter, bandstop filter, coupled line structure, quasi-absorptive filter, quasi-reflectionless filter, T-shaped microstrip structure.

I. INTRODUCTION

BANDPASS filter (BPF) and bandstop filter (BSF) are two of the most fundamental components in radio-frequency identification (RFID) [1]–[3] and communication systems [4], [5]. In the past decades, various BPFs and BSFs with good performance were designed using multimode resonators [6], [7], parallel coupled-line structures [8]–[10]

Manuscript received May 19, 2021; revised July 9, 2021 and August 9, 2021; accepted August 18, 2021. Date of publication August 25, 2021; date of current version December 27, 2021. This work was supported in part by the NSAF Joint Fund under Grant U2130102; in part by the FY2019 JSPS Postdoctoral Fellowship for Research in Japan under Grant P19350; in part by the Natural Science Foundation of Shaanxi Province of China under Grant 2021JQ-060; and in part by the “Siyuan Scholar” Fellowship of XJTU. (Corresponding author: Kai-Da Xu.)

Kai-Da Xu is with the School of Information and Communications Engineering, Xi’an Jiaotong University, Xi’an 710049, China, and also with the Department of Communications Engineering, Graduate School of Engineering, Tohoku University, Sendai 980-8579, Japan (e-mail: kaidaxu@ieee.org).

Sen Lu is with the Department of Electronic Science, Xiamen University, Xiamen 361005, China.

Ying-Jiang Guo is with the Microsystem and Terahertz Research Center, China Academy of Engineering Physics, Chengdu 610200, China.

Qiang Chen is with the Department of Communications Engineering, Graduate School of Engineering, Tohoku University, Sendai 980-8579, Japan. Digital Object Identifier 10.1109/JRFID.2021.3106664

and so on. In all these conventional filters, the signals at pass-band region transmit to output terminals while the signals at stopband region reflect back to the source, which perhaps deteriorate the characteristics of other microwave components in RF front-end systems. Consequently, a new type of filters, i.e., reflectionless filter or absorptive filter [11], has been emerged, which dissipates the reflected signals in lossy components rather than reflecting back to the input port.

In recent years, reflectionless or quasi-reflectionless (QR) filters using different techniques and approaches have been explored. In theory, the reflectionless filter performs the ideal null power reflection in the frequency range of interest [12]–[18]. Based on odd- and even-mode circuit analysis, a class of reflectionless filter prototypes with lowpass, highpass, bandpass and bandstop characteristics were realized by lumped elements in [12], and then implemented using transmission lines in [13]–[14]. Besides, in [15], the coupling matrix derived from the proposed complementary duplexer architectures was used to synthesize input-reflectionless adaptive filters in bandpass, bandstop, and cascade designs. Afterwards, several extended works including tunable reflectionless BPFs [16], multiband reflectionless filters [17] and dual-behavior reflectionless BPFs [18] were investigated.

In addition to input-reflectionless filters, i.e., single-port reflectionless filters [15]–[18], two-port QR filters were further explored [19]–[22], which can achieve QR behaviors at their two ports. Under the rigorous theoretical analysis, symmetrical QR BSF [19] and BPF [20] were introduced, respectively, with better performance in high-order realizations. For the design in [21], its frequency selectivity could be improved by cascading multiple bandpass sections without affecting its bandwidth. Two complementary sections were developed to construct the QR filters in [22], but the design procedures were not synthesized. More recently, several QR filters with novel features have been investigated, such as constant absolute bandwidth [23]–[24], independently controllable dual passband [25], and balanced characteristics [26]. With the increasing integration of RF system, the QR filters will be extremely desirable. It is necessary to introduce a type of QR filters with simple topology as well as the detailed design procedure.

In this paper, a new class of single- and two-port QR filters, using simple coupled line and T-shaped microstrip structures, are presented systematically for the applications in RFID [3] or other systems. First, bandpass filtering response of the coupled line structure and bandstop filtering response of the T-shaped

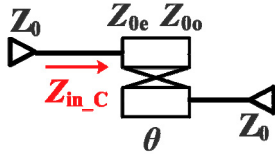


Fig. 1. The circuit detail of the coupled line structure (electrical length $\theta = 90^\circ$ at center frequency f_0 , and port characteristic impedance $Z_0 = 50\Omega$).

microstrip structure are analyzed in details in Section II. Then, single- and two-port QR filters (including BPFs and BSFs) are proposed in Sections III and IV, respectively, where the identical 3-dB fractional bandwidth (FBW) of the two structures is used as the quasi-complementary condition for the design guidance. After that, in Section V, the design procedures for these four types of QR filters are summarized and two prototypes of the two-port QR filters are fabricated and measured to validate the proposed approach. Finally, a brief conclusion of this paper is provided in Section VI.

II. COUPLED LINE AND T-SHAPED MICROSTRIP STRUCTURES

In this section, two simple structures, i.e., coupled line structure and T-shaped microstrip structure, are presented and analyzed to achieve the bandpass and bandstop filtering responses, respectively. They can be utilized together for the design of the QR filters.

A. Coupled Line Structure

Fig. 1 shows a simple structure using a pair of quarter-wavelength coupled lines, with odd- and even-mode characteristic impedances of Z_{0o} and Z_{0e} , respectively. According to the impedance matrix $[Z]$ of coupled lines [27], the input impedance Z_{in_C} of this structure terminated by the load impedance Z_0 can be calculated by

$$Z_{in_C} = \frac{(Z_{0e} - Z_{0o})^2 \csc^2 \theta}{4Z_0 - j2(Z_{0e} + Z_{0o}) \cot \theta} - \frac{j(Z_{0e} + Z_{0o}) \cot \theta}{2} \quad (1)$$

Besides, the coupling coefficient (k) of the coupled lines is defined as

$$k = \frac{Z_{0e} - Z_{0o}}{Z_{0e} + Z_{0o}} \quad (2)$$

By replacing the Z_{0e} in (1) with Z_{0o} and k based on (2), the new expression of the input impedance Z_{in_C} is shown as

$$Z_{in_C} = \frac{Z_{0o}}{k-1} \left[\frac{k^2 Z_{0o}}{(kZ_0 - Z_0 + jZ_{0o} \cot \theta) \sin^2 \theta} + j \cot \theta \right] \quad (3)$$

The magnitudes of reflection coefficient (S_{11_C}) and transmission coefficient (S_{21_C}) of the coupled line structure can be expressed by

$$|S_{11_C}| = \left| \frac{Z_{in_C} - Z_0}{Z_{in_C} + Z_0} \right| \quad (4a)$$

$$|S_{21_C}| = \sqrt{1 - |S_{11_C}|^2} \quad (4b)$$

Base on the theoretical expressions above, the property of the coupled line structure is determined by the parameters of Z_{0o} and k . The coupled line structure can realize the adjustable

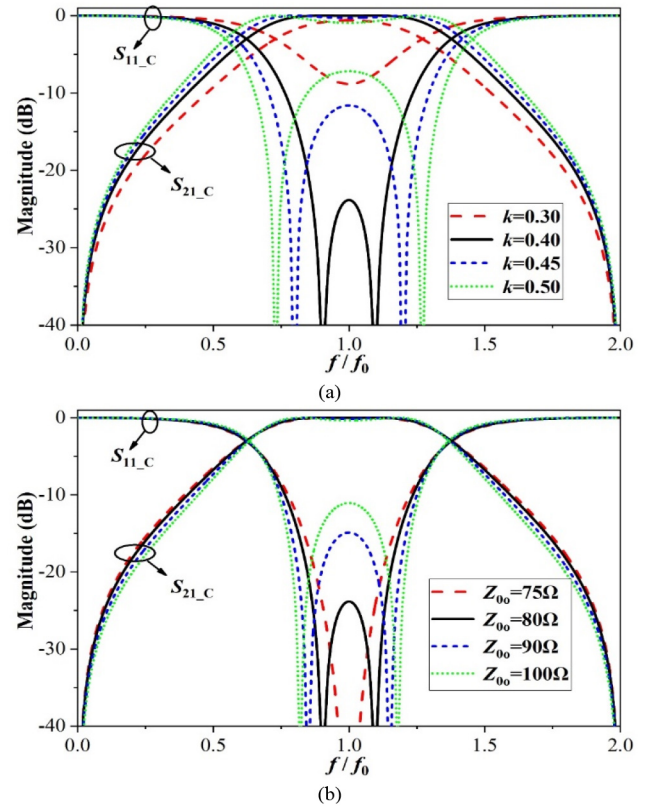


Fig. 2. Simulated S -parameters of the coupled line structure (a) with different k when $Z_{0o} = 80 \Omega$ is fixed, and (b) with different Z_{0o} when $k=0.4$ is fixed.

bandpass filtering response as long as the suitable parameter values of Z_{0o} and k are set, which will be analyzed below.

In order to give a clear design insight, herein, the parametric studies of k and Z_{0o} are shown in Fig. 2. When $Z_{0o} = 80 \Omega$ is fixed, the S -parameters of coupled line structure with varied k are illustrated in Fig. 2(a). As the coupling coefficient k increases, a pair of transmission poles are generated and moved away from f_0 , leading to wider FBW of the passband and varied in-band return loss. When $k = 0.4$ is fixed, the S -parameters of coupled line structure with different Z_{0o} are exhibited in Fig. 2(b), in which the varied Z_{0o} only affects the in-band return loss while the passband FBW almost keep unchanged. Accordingly, for realizing an adjustable bandpass filtering response, the passband FBW of coupled line structure can be firstly determined by the coupling coefficient k , and subsequently the in-band return loss can be optimized by the odd-mode characteristic impedance Z_{0o} with little influence on the design specification of FBW. According to the discussions above, we acquire the relations between the 3-dB passband FBW (Δf_C) of the coupled line structure and the parameters (k and Z_{0o}), with the fixed in-band return loss of 20 dB, which are illustrated in Fig. 3(a). As can be seen, we should increase k and decrease Z_{0o} simultaneously to broaden Δf_C with the fixed in-band return loss. From the Fig. 3(a), we can conveniently determine the corresponding parameters of k and Z_{0o} for the required cases. Three cases, named as Cases A1, A2 and A3, with Δf_C of 60%, 80% and 100%, respectively, are marked in Fig. 3(a). Their S -parameters are plotted in Fig. 3(b). The coupled line structure will be useful to be as a BPF section in the construction of QR filters.

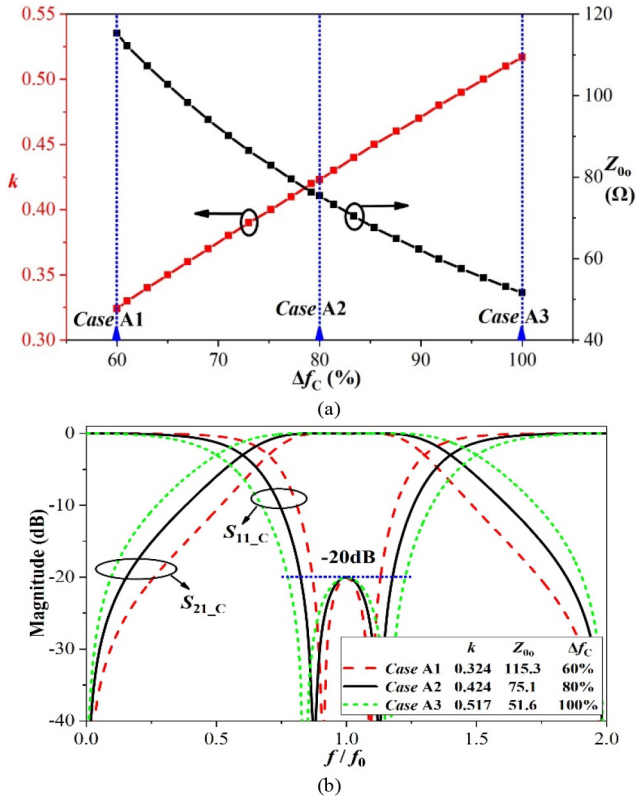


Fig. 3. (a) Relations between the 3-dB passband FBW (Δf_C) and the parameters of the coupled lines (k and Z_{00}) with the fixed in-band return loss of 20 dB. (b) S-parameters of the coupled line structure in Case A1, Case A2 and Case A3.

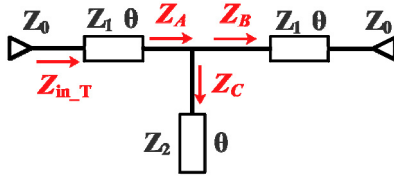


Fig. 4. The circuit detail of the T-shaped microstrip structure (electrical length $\theta=90^\circ$ at center frequency f_0 , and port characteristic impedance $Z_0=50 \Omega$).

B. T-Shaped Microstrip Structure

Fig. 4 shows another simple structure, namely, T-shaped microstrip structure, where a quarter-wavelength open-ended stub (characteristic impedance Z_2) is loaded in the middle of a half-wavelength microstrip line (characteristic impedance Z_1). The input impedance Z_{in_T} of the T-shaped microstrip structure terminated by Z_0 can be obtained as

$$Z_{in_T} = Z_1 \frac{Z_A + jZ_1 \tan \theta}{Z_1 + jZ_A \tan \theta} \quad (5)$$

where

$$Z_A = Z_B // Z_C, \quad Z_B = Z_1 \frac{Z_0 + jZ_1 \tan \theta}{Z_1 + jZ_0 \tan \theta}, \quad Z_C = -jZ_2 \cot \theta \quad (6)$$

The impedance ratio (m) of the two transmission lines is defined as

$$m = \frac{Z_2}{Z_1} \quad (7)$$

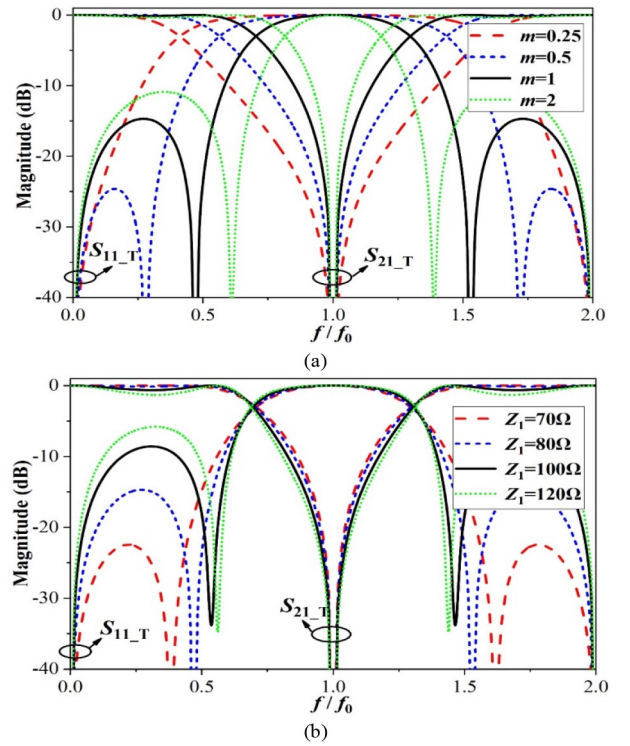


Fig. 5. Simulated S-parameters of the T-shaped microstrip structure (a) with different m when $Z_1 = 80 \Omega$ is fixed, and (b) with different Z_1 when $m = 1$ is fixed.

By replacing the Z_2 in (5) and (6) with Z_1 and m based on (7), the new expression of input impedance Z_{in_T} is shown as

$$Z_{in_T} = Z_1 \frac{Z_0(m - m \tan^2 \theta - \tan^2 \theta) + jZ_1(2m - \tan^2 \theta) \tan \theta}{Z_1(m - m \tan^2 \theta - \tan^2 \theta) + jZ_0(1 + 2m) \tan \theta} \quad (8)$$

Consequently, the magnitude of reflection coefficient (S_{11_T}) and transmission coefficient (S_{21_T}) of the T-shaped microstrip structure can be expressed by

$$|S_{11_T}| = \left| \frac{Z_{in_T} - Z_0}{Z_{in_T} + Z_0} \right| \quad (9a)$$

$$|S_{21_T}| = \sqrt{1 - |S_{11_T}|^2} \quad (9b)$$

Base on the theoretical expressions above, the property of the T-shaped microstrip structure is determined by the parameters of Z_1 and m . The T-shaped microstrip structure can realize the adjustable bandstop filtering response as long as the suitable parameter values of Z_1 and m are set, which will be analyzed below.

The parametric studies of m and Z_1 are also made for the T-shaped microstrip structure, as shown in Fig. 5. Seen from Fig. 5(a), as the impedance ratio m increases with fixed $Z_1 = 80 \Omega$, a pair of new transmission poles are generated and moved close to f_0 , resulting in narrower stopband FBW and worse out-of-band return loss. When $m = 1$ is fixed, the S-parameters of T-shaped microstrip structure with different Z_1 are shown in Fig. 5(b), in which the varied Z_1 will only affects the out-of-band return loss while the stopband FBW almost remains unchanged. Therefore, for realizing tunable bandstop

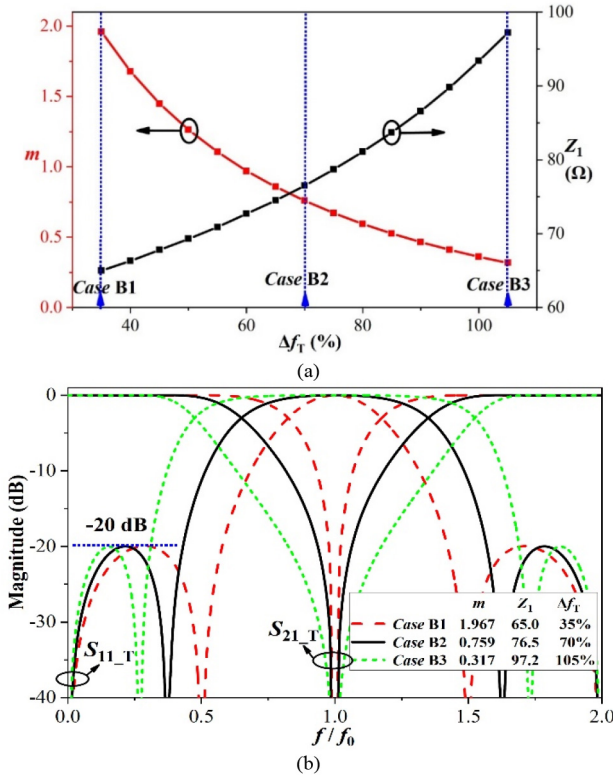


Fig. 6. (a). Relations between the 3-dB stopband FBW (Δf_T) and the parameters of T-shaped microstrip structure (m and Z_1) with the fixed out-of-band return loss of 20 dB. (b) S -parameters of the T-shaped microstrip structure in Case B1, Case B2 and Case B3.

filtering response, the stopband FBW of T-shaped microstrip structure can be firstly determined by the impedance ratio m , and then the out-of-band return loss can be further optimized by changing the characteristic impedance Z_1 .

Similarly, we can also obtain the relations between the 3-dB stopband FBW (Δf_T) and the parameters of T-shaped microstrip structure (m and Z_1), with the fixed out-of-band return loss of 20 dB, as shown in Fig. 6(a). If the Δf_T needs to be broadened, we can increase the parameter m and decrease Z_1 simultaneously. Three cases (i.e., Cases B1, B2 and B3) with Δf_T of 35%, 70% and 105%, respectively, are taken for instance, marked in Fig. 6(a). Their simulated S -parameters are plotted in Fig. 6(b). According to the analysis above, the T-shaped microstrip structure will be suitable as a BSF section for the design of QR filters.

III. SINGLE-PORT QR BPF AND BSF

In this section, the single-port QR BPF and BSF are proposed based on the complementary-duplexer arrangement of the two mentioned structures, in which the 3-dB pass-band FBW of coupled line structure and 3-dB stopband FBW of T-shaped microstrip structure are set identically as the quasi-complementary condition for the design guidance, i.e., $\Delta f_C = \Delta f_T$.

Fig. 7 demonstrates the single-port QR BPF and BSF to achieve the QR behaviors at input ports (Port 1). The output port of the T-shaped microstrip structure is replaced with

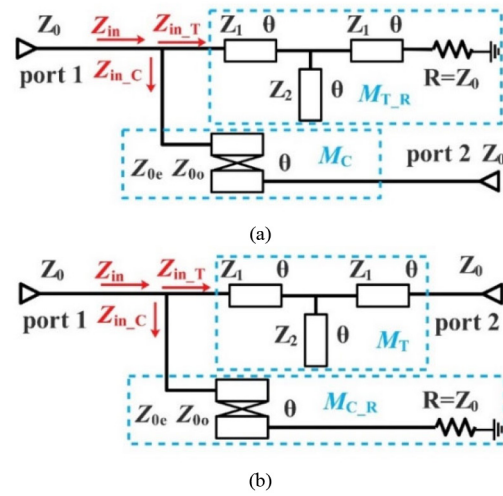


Fig. 7. Circuit schematics of the proposed single-port QR (a) BPF and (b) BSF.

a lossy resistor $R (= Z_0)$ to realize the single-port QR BPF as shown in Fig. 7(a). On the contrary, the output port of the coupled line structure is replaced with the resistor R for constructing the single-port QR BSF as seen in Fig. 7(b). The performance of the single-port QR BPF and BSF can be directly visualized from their S -parameters, which are able to be derived from the corresponding $ABCD$ matrices.

The overall $ABCD$ matrix of the single-port QR BPF is equal to $M_{T,R} \times M_C$, where $M_{T,R}$ and M_C are the $ABCD$ matrices of T-shaped microstrip structure (terminated by resistor R) and coupled lines, respectively, expressed as [27]

$$M_{T,R} = \begin{bmatrix} 1 & 0 \\ 1/Z_{in,T} & 1 \end{bmatrix} \quad (10a)$$

$$M_C = \begin{bmatrix} \frac{\cos \theta}{k} & jZ_{0o} \frac{k^2 - \cos^2 \theta}{k(1-k) \sin \theta} \\ j \frac{(1-k) \sin \theta}{kZ_{0o}} & \frac{\cos \theta}{k} \end{bmatrix} \quad (10b)$$

Similarly, the overall $ABCD$ matrix of the single-port QR BSF is expressed as $M_{C,R} \times M_T$, where $M_{C,R}$ and M_T are the $ABCD$ matrices of the coupled line structure (terminated by resistor R) and the T-shaped microstrip line, respectively, which can be calculated as [27]

$$M_{C,R} = \begin{bmatrix} 1 & 0 \\ 1/Z_{in,C} & 1 \end{bmatrix} \quad (11a)$$

$$M_T = \begin{bmatrix} \cos 2\theta - \frac{\sin^2 \theta}{m} & jZ_1 (\sin 2\theta - \frac{\sin^3 \theta}{m \cos \theta}) \\ j \frac{(1+2m) \sin 2\theta}{2mZ_1} & \cos 2\theta - \frac{\sin^2 \theta}{m} \end{bmatrix} \quad (11b)$$

After the conversion from $ABCD$ - to S -parameters, the reflection coefficient S_{11} and transmission coefficient S_{21} of the single-port QR BPF (or BSF) can be expressed as

$$S_{11} = \frac{AZ_0 + B - CZ_0^2 - DZ_0}{AZ_0 + B + CZ_0^2 + DZ_0} \quad (12a)$$

$$S_{21} = \frac{2Z_0}{AZ_0 + B + CZ_0^2 + DZ_0} \quad (12b)$$

where the parameters A , B , C , and D are the corresponding entries of $ABCD$ matrix.

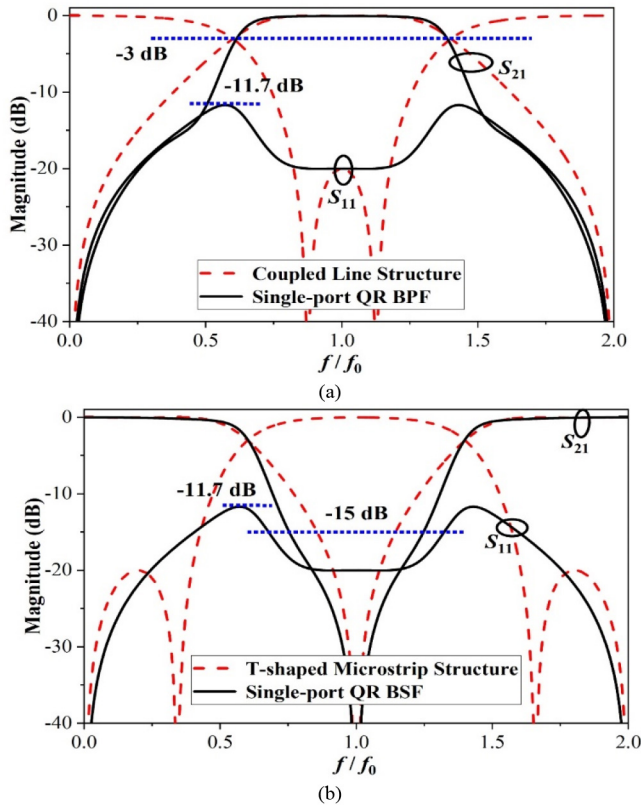


Fig. 8. S -parameters of the single-port QR (a) BPF and (b) BSF with the parameters of $Z_{00} = 75.1\Omega$, $k = 0.424$, $Z_1 = 81.1\Omega$, and $m = 0.594$.

According to the analysis above, Figs. 8(a) and (b) plot the S -parameters of the single-port QR BPF and BSF in Fig. 7 with $\Delta f_C = \Delta f_T = 80\%$. Once the 3-dB FBW of the design specifications is chosen, all the parameter variables in Fig. 7 can be straightforwardly extracted from Fig. 3(a) and Fig. 6(a). Also, the corresponding S -parameters of coupled line and T-shaped microstrip structures are plotted in Figs. 8(a) and (b) for reference, respectively, where the unwanted signals are reflected to input ports. In contrast, the single-port QR BPF and BSF have the QR behaviors, where the reflection coefficients (S_{11}) are better than -11.7 dB from 0 to $2f_0$, meaning that the reflected signals are effectively dissipated in the lossy resistors. Moreover, as seen in Fig. 8(a), the selectivity of the single-port QR BPF is improved obviously compared with that of the coupled line structure, due to the adding absorption channel. This advantage also exists in the single-port QR BSF. Besides, the 15-dB stopband FBW of the single-port QR BSF is 49.4%, much larger than that of the T-shaped microstrip structure as shown in Fig. 8(b). In addition, the reflection coefficients of the single-port QR BPF and BSF, could be adjusted by changing Z_{00} , with little influence on the specified FBW. The out-of-band rejection and band-edge selectivity can be improved by cascading more orders.

In order to design the single-port QR BPF and BSF conveniently, the FBWs of single-port QR BPF and BSF against the varied Δf are exhibited in Fig. 9, where $\Delta f = \Delta f_C = \Delta f_T$. The 3-dB passband FBW of coupled line structure and 3-dB stopband FBW of T-shaped structure are set identically, i.e., Δf , changing from 60% to 100%. Over this range, the single-port

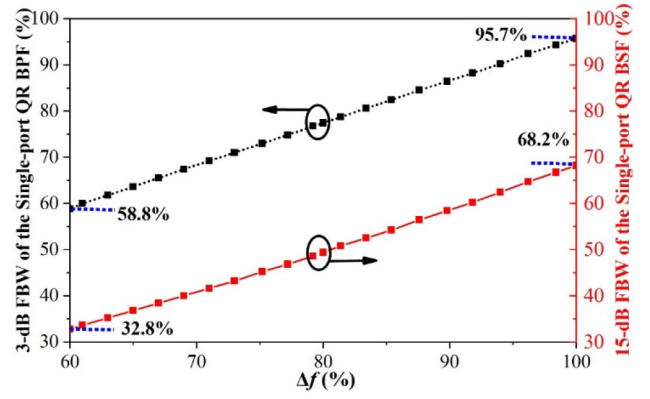


Fig. 9. FBWs of the single-port QR BPF and BSF with different Δf , where $\Delta f = \Delta f_C = \Delta f_T$.

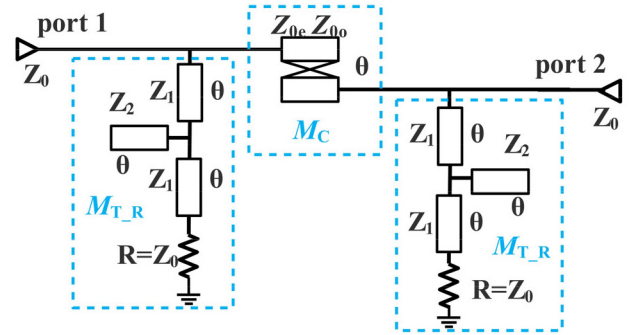


Fig. 10. Circuit schematic of the proposed two-port QR BPF.

QR BPF has the tunable 3-dB FBW from 58.8% to 95.7%, while the single-port QR BSF possesses the tunable 15-dB FBW varying from 32.8% to 68.2%. In other words, any case within these ranges can be readily designed, guided from Fig. 9.

IV. TWO-PORT QR BPF AND BSF

In this section, based on the single-port QR filters, two-port QR BPF and BSF are constructed through loading additional T-shaped microstrip structure and coupled line structure with the resistor R as the absorption channel for the output port, respectively. The characteristics of two-port QR filters are analyzed and compared with those of single-port QR filters.

A. Two-Port QR BPF

Fig. 10 shows the circuit schematic of the proposed two-port QR BPF, where an additional absorption channel is loaded near the output port based on the architecture of the single-port QR BPF. Two bilateral absorption channels will effectively dissipate the unwanted signals to realize the two-port QR behaviors. Due to configuration in symmetry, the two ports have the same characteristics.

The performance of the two-port QR BPF can be straightforwardly seen from its S -parameters, while the S -parameters can be converted from the corresponding $ABCD$ matrix. According to the cascaded principle, the overall $ABCD$ matrix of two-port QR BPF in Fig. 10 is expressed as $M_{T_R} \times M_C \times M_{T_R}$.

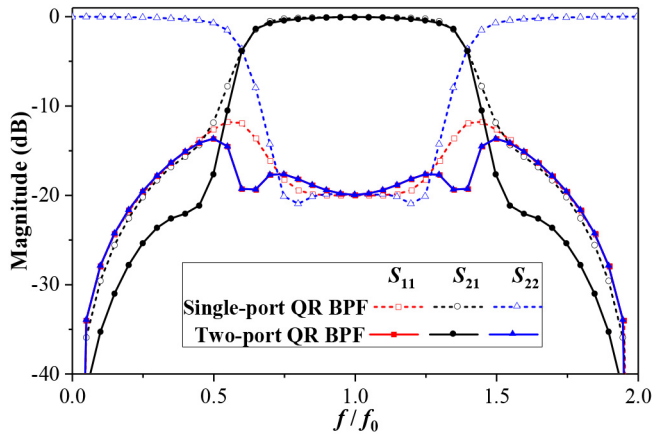


Fig. 11. S -parameters of the single- and two-port QR BPFs when the Δf is selected as 80%.

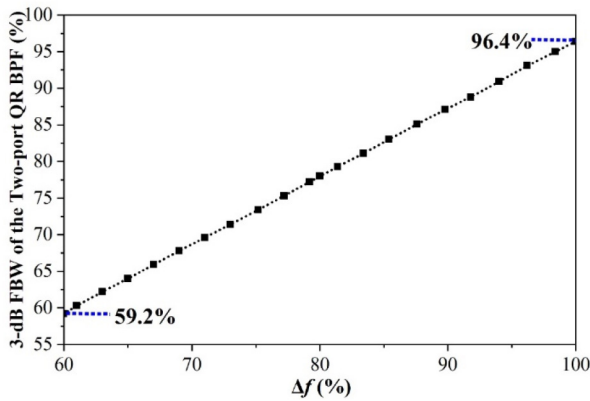


Fig. 12. The 3-dB FBW of the two-port QR BPF with varied Δf , where $\Delta f = \Delta f_C = \Delta f_T$.

Consequently, the S -parameters can be obtained using (12a) and (12b). For demonstration, the Δf is chosen as 80% with a set of corresponding parameters extracted from Figs. 3(a) and 6(a), i.e., $Z_{00} = 75.1\Omega$, $k = 0.424$, $Z_1 = 81.1\Omega$, and $m = 0.594$. Fig. 11 depicts the S -parameters of the two-port QR BPF for the case of $\Delta f = 80\%$, as well as those of the single-port QR BPF for comparisons. The two-port QR BPF not only has the QR behaviors at both of the input and output ports, but also has improved performance, including better selectivity and reflectionless effect. In addition, the method to further enhance reflectionless effect through tuning the parameter Z_{00} , k , Z_1 , or m as mentioned in Section III, is also suitable for two-port QR BPF.

Note that the 3-dB FBW of the two-port QR BPF is 78%, slightly different from $\Delta f = 80\%$. In order to design the two-port QR BPF conveniently, Fig. 12 plots the 3-dB FBW of two-port QR BPF with varied Δf . Considering the quasi-complementary condition for the coupled line and T-shaped microstrip structures in Section III-A, the overlapped 3-dB FBW region from 60% to 100% is chosen for the range of Δf . Within this range, the 3-dB FBW of the two-port QR BPF is varied from 59.2% to 96.4%. Any case of two-port QR BPFs within this 3-dB FBW range can be readily designed using the proposed method.

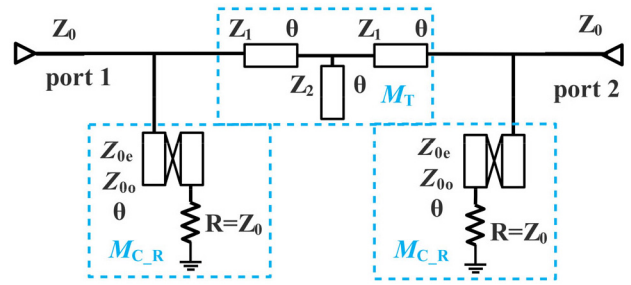


Fig. 13. Circuit schematic of the two-port QR BSF.

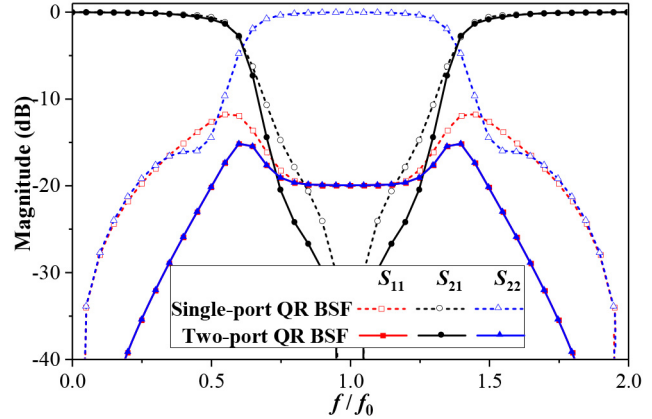


Fig. 14. S -parameters of the single- and two-port QR BSFs when the Δf is selected as 80%.

B. Two-Port QR BSF

Fig. 13 presents the circuit schematic of the proposed two-port QR BSF which is developed from single-port QR BSF, just with an additional absorption channel loaded at output port. Thus, two bilateral absorption channels will effectively dissipate the undesired signals at both of input and output ports.

Similarly, the S -parameters of the two-port QR BSF can be also converted from the corresponding $ABCD$ matrix, which is equal to $M_{C,R} \times M_T \times M_{C,R}$ according to the cascaded principle. For demonstration, the Δf is selected as 80%, identical to the example of two-port QR BPF above. Fig. 14 depicts the S -parameters of the single- and two-port QR BSFs when $\Delta f = 80\%$. Compared with the single-port QR BSF, the two-port QR BSF possesses the reflectionless effect at both of the input and output ports. Moreover, the frequency selectivity within the stopband and reflection coefficients from 0 to $2f_0$ are also better than those of the single-port QR BSF. The 15-dB stopband FBW of the two-port QR BSF is 59.2%, obviously larger than that of the single-port QR BSF, which is 49.4%.

To facilitate the design of the two-port QR BSF, Fig. 15 shows the 15-dB stopband FBW of the two-port QR BSF with varied Δf . As the Δf ranges from 60% to 100%, the 15-dB FBW of the two-port QR BSF is changed from 43.3% to 76.6%. Accordingly, any case within this 15-dB FBW range can be readily designed following the introduced approach.

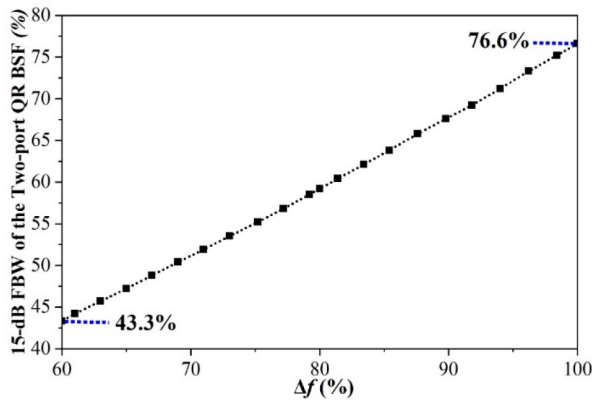


Fig. 15. The 15-dB stopband FBW of the two-port QR BSF with varied Δf , where $\Delta f = \Delta f_C = \Delta f_T$.

V. DESIGN PROCEDURE AND IMPLEMENTATION RESULTS

Four types of QR filters, including single- and two-port QR BPFs, and single- and two-port QR BSFs, have been proposed and analyzed using simple coupled line and T-shaped microstrip structures. It is feasible to design the required single- and two-port QR BPFs with the 3-dB FBWs in the ranges of 58.8%-95.7% and 59.2%-96.4%, respectively, and the single- and two-port QR BSFs with the 15-dB FBWs in the ranges of 32.8%-68.2% and 43.3%-76.6%, respectively.

A simple design procedure for the proposed QR filters is summarized as the following steps.

1) Select the type of the QR filter, and choose the desired center frequency f_0 and the bandwidth (3-dB FBW for BPF and 15-dB FBW for BSF) according to the design specifications.

2) Obtain the corresponding Δf once the desired bandwidth is determined, according to Fig. 9 for the design of single-port QR BPF or BSF, and Figs. 12 and 15 for the design of the two-port QR BPF and BSF, respectively.

3) According to $\Delta f_C = \Delta f_T = \Delta f$, extract the parameters Z_{0o} and k of the coupled line structure from Fig. 3(a) and Z_1 and m of the T-shaped microstrip structure from Fig. 6(a).

4) Convert the electrical length θ and four characteristic impedances Z_{0o} , Z_{0e} , Z_1 and Z_2 to the corresponding physical dimensions of the coupled line and T-shaped microstrip structures. These dimensions of QR filter are further fine-tuned in full-wave electromagnetic simulations to account for the unintended coupling effects among the transmission lines.

For demonstrations, a two-port QR BPF with the targeted 3-dB FBW of 70% and a two-port QR BSF with the targeted 15-dB FBW of 50% as samples are designed and implemented using the proposed method. The center frequencies of them are both operated at 2 GHz.

For the two-port QR BPF, the targeted 3-dB FBW of 70% corresponds to the Δf of 71.6%, extracted from Fig. 12. Then, a set of electrical parameters $Z_{0o} = 89.4\Omega$, $k = 0.382$, $Z_1 = 77.2\Omega$, and $m = 0.729$ can be directly acquired from Figs. 3(a) and 6(a). Fig. 16 shows the simulated S -parameters of the two-port QR BPF in this configuration. It is found that two ports have superior bandpass filtering property and reflection coefficient of better than -14.2 dB from 0 to 4 GHz.

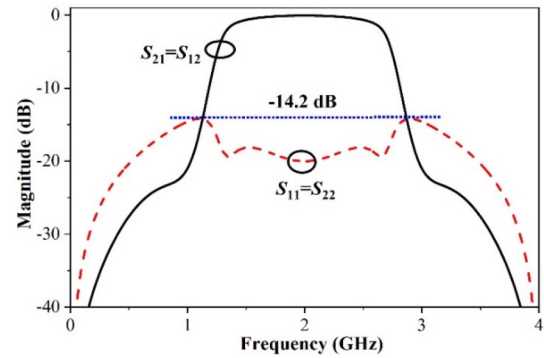


Fig. 16. Simulated S -parameters of the two-port QR BPF using extracted electrical parameters, where $Z_{0o} = 89.4\Omega$, $k = 0.382$, $Z_1 = 77.2\Omega$, and $m = 0.729$.

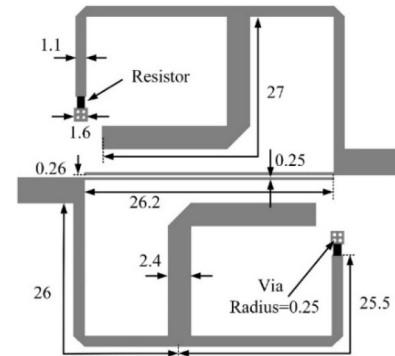


Fig. 17. Layout of the designed two-port QR BPF (unit: mm).

Subsequently, the electrical length and characteristic impedances are converted to the corresponding physical dimensions of the two-port QR BPF, which is designed on an F4B substrate with a relative permittivity of $\epsilon_r = 2.65$ and a dielectric thickness of $h = 1$ mm. The layout of the two-port QR BPF and its final dimensions after the fine-tuning process in full-wave simulation software Ansys HFSS are shown in Fig. 17. A prototype of the two-port QR BPF has been fabricated and tested. Two 100- Ω resistors are stacked and welded together to obtain the shunt resistance value of 50 Ω due to the fact that the 50- Ω chip resistor is not available in the commercial market. The simulations and measurements of the two-port QR BPF are in good agreement, as shown in Fig. 18. The measured 3-dB FBW is 73.2% (1.29 ~ 2.78 GHz) with a center frequency of 2.035 GHz, reasonably coincident with the required design specification. The minimum insertion loss is 0.4 dB within the passband, and the return losses are all better than 12.9 dB ranged from 0 to 4 GHz.

For the design of two-port QR BSF, the targeted 15-dB FBW of 50% corresponds to the Δf of 68.6%, which is extracted from Fig. 15. Consequently, the four electrical parameters will be straightforwardly obtained from Figs. 3(a) and 6(a), namely, $Z_{0o} = 94.9\Omega$, $k = 0.368$, $Z_1 = 76\Omega$, and $m = 0.783$. The simulated S -parameters for the two-port QR BSF are exhibited in Fig. 19 with good bandstop filtering property and reflection coefficient of better than -15.5 dB from 0 to 4 GHz.

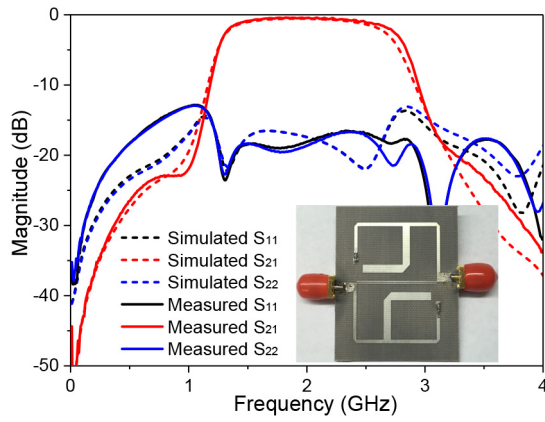


Fig. 18. Simulated and measured results of the two-port QR BPF along with the inset photograph of the fabricated prototype.

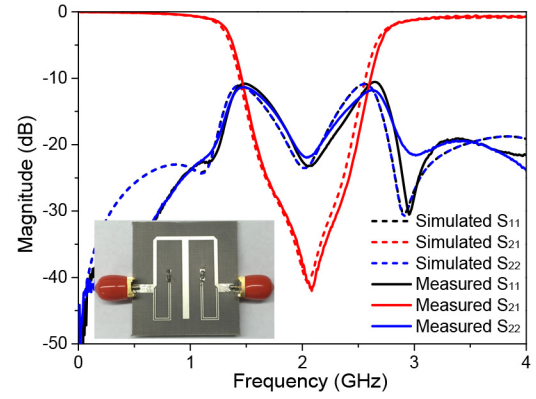


Fig. 21. Simulated and measured results of the two-port QR BSF along with the inset photograph of the fabricated prototype.

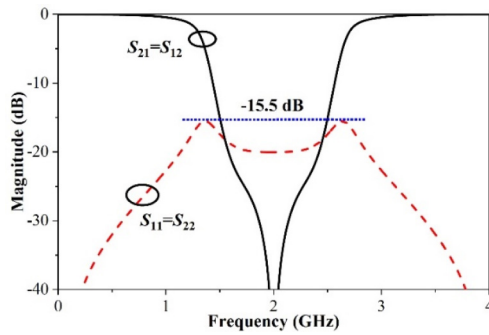


Fig. 19. Simulated S -parameters of the two-port QR BSF using extracted electrical parameters, where $Z_{0o} = 94.9\Omega$, $k = 0.368$, $Z_1 = 76\Omega$, and $m = 0.783$.

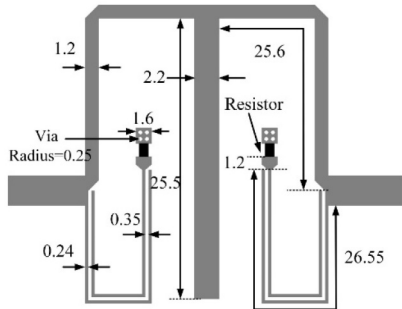


Fig. 20. Layout of the designed two-port QR BSF (unit: mm).

The final layout of the two-port QR BSF can be constructed through converting the ideal parameters to the corresponding physical dimensions, as shown in Fig. 20, where the same F4B substrate is employed as mentioned above. Fig. 21 illustrates the simulated and measured results of the two-port QR BSF along with the inset photograph of the fabricated prototype, where the $50\text{-}\Omega$ lossy resistors are obtained using two stacked $100\text{-}\Omega$ chip resistors. The measurements agree well with the simulations as seen in Fig. 21, and the measured 15-dB FBW is 50.4% ($1.52 \sim 2.55$ GHz) with a center frequency of 2.035 GHz, consistent with the targeted design specification. Within the stopband, the maximum rejection level and reflectionless effect are -41.6 dB and -22 dB, respectively. Moreover, the measured reflection coefficients of the two ports

TABLE I
COMPARISONS WITH SOME PREVIOUS WORKS

	Number of QR port	Filter type	Test band (GHz)	3-dB passband FBW / 15-dB stopband FBW	10-dB Reflection level FBW	Design steps
[18]	Single	BPF	1-3	8.8%	81% (1.25-2.71 GHz)	No
[21]-I	Two	BPF	1-7	22.5%	Covering all test band	Yes
[22]-I	Two	BPF	0.5-3.5	27%	111% (0.82-3.03 GHz)	No
[28]-I	Single	BPF	1-3	8.5%	74% (1.33-2.81 GHz)	Yes
[28]-II	Single	BPF	1-3	20.5%	61% (1.44-2.66 GHz)	Yes
This work-I	Two	BPF	0-4	73.2%	Covering all test band	Yes
This work-II	Two	BSF	0-4	50.4%	Covering all test band	Yes

are below -11.9 dB and -10.8 dB, respectively, within the frequency range from 0 to 4 GHz. Additionally, in order to alleviate the passband-rounding effect, the higher-order complementary sections as absorption channel with regard to the transmission channel [28], or the loss consideration in the transmission lines through introducing the attenuation constant [29] can be adopted.

Finally, Table I tabulates a comparison with some previous works. It is found that our work is helpful to design both of the QR BPF and BSF. The two samples present wide FBW and good power-matching level. Moreover, the design procedure is provided to design the QR filters with required specifications.

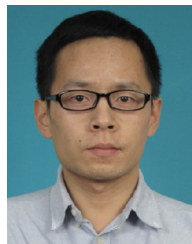
VI. CONCLUSION

Four types of QR filters, including single- and two-port QR BPFs and BSFs, have been designed and analyzed using the combinations of the coupled line and T-shaped microstrip structures. To guide and facilitate the design of the QR

filters, identical 3-dB FBW of the above-mentioned two structures as the quasi-complementary condition has been applied. Furthermore, detailed design procedures have been summarized and two fabricated cases have been measured to validate the proposed idea. Due to the simple structures and design method, the proposed work may have promising potential applications in stable RFID and 5G communication systems.

REFERENCES

- [1] N. Soltanieh, Y. Norouzi, Y. Yang, and N. C. Karmakar, "A review of radio frequency fingerprinting techniques," *IEEE J. Radio Freq. Identif.*, vol. 4, no. 3, pp. 222–233, Sep. 2020.
- [2] Y. Song, P. Wen, H. Liu, Y. Wang, and L. Geng, "Design of compact balanced-to-balanced diplexer using dual-mode CRLH resonator for RFID and 5G applications," *IEEE J. Radio Freq. Identif.*, vol. 3, no. 3, pp. 143–148, Sep. 2019.
- [3] M. M. Forouzandeh, J. Aliasgari, and N. Karmakar, "A wideband directive filter for LO leakage reduction in UWB frequency-domain chipless RFID readers," in *Proc. IEEE Int. Conf. RFID (RFID)*, Atlanta, GA, USA, 2021, pp. 1–5.
- [4] Y.-J. Guo, K.-D. Xu, X. Deng, X. Cheng, and Q. Chen, "Millimeter-wave on-chip bandpass filter based on spoof surface plasmon polaritons," *IEEE Electron Device Lett.*, vol. 41, no. 8, pp. 1165–1168, Aug. 2020.
- [5] K.-D. Xu, Y. Guo, Y. Liu, X. Deng, Q. Chen, and Z. Ma, "60-GHz compact dual-mode on-chip bandpass filter using GaAs technology," *IEEE Electron Device Lett.*, vol. 42, no. 8, pp. 1120–1123, Aug. 2021.
- [6] J. Ai, Y. Zhang, K. Xu, D. Li, and Y. Fan, "Miniaturized quint-band bandpass filter based on multi-mode resonator and $\lambda/4$ resonators with mixed electric and magnetic coupling," *IEEE Microw. Wireless Compon. Lett.*, vol. 26, no. 5, pp. 343–345, May 2016.
- [7] J. Ai, Y. H. Zhang, K. D. Xu, M. K. Shen, and W. T. Joines, "Miniaturized frequency controllable bandstop filter using coupled line stubs loaded shorted SIR for tri-band application," *IEEE Microw. Wireless Compon. Lett.*, vol. 27, no. 7, pp. 627–629, Jul. 2017.
- [8] Y. Wu, L. Cui, Z. Zhuang, W. Wang, and Y. Liu, "A simple planar dual-band bandpass filter with multiple transmission poles and zeros," *IEEE Trans. Circuits Syst. II, Exp. Briefs*, vol. 65, no. 1, pp. 56–60, Jan. 2018.
- [9] Y. Cai, K. D. Xu, Z. Ma, and Y. Liu, "Compact bandstop filters using coupled lines and open/short stubs with multiple transmission poles," *IET Microw. Antennas Propag.*, vol. 13, no. 9, pp. 1368–1372, Jul. 2019.
- [10] K. D. Xu, D. Li, and Y. Liu, "High-selectivity wideband bandpass filter using simple coupled lines with multiple transmission poles and zeros," *IEEE Microw. Wireless Compon. Lett.*, vol. 29, no. 2, pp. 107–109, Feb. 2019.
- [11] J.-Y. Shao and Y.-S. Lin, "Narrowband coupled-line bandstop filter with absorptive stopband," *IEEE Trans. Microw. Theory Techn.*, vol. 63, no. 10, pp. 3469–3478, Oct. 2015.
- [12] M. A. Morgan and T. A. Boyd, "Theoretical and experimental study of a new class of reflectionless filter," *IEEE Trans. Microw. Theory Techn.*, vol. 59, no. 5, pp. 1214–1221, May 2011.
- [13] M. A. Morgan and T. A. Boyd, "Reflectionless filter structures," *IEEE Trans. Microw. Theory Techn.*, vol. 63, no. 4, pp. 1263–1271, Apr. 2015.
- [14] C. Jackson, "Transmission line replacements for a lumped element reflectionless filter," in *Proc. Radio Wireless Symp.*, San Diego, CA, USA, Jan. 2014, pp. 166–168.
- [15] D. Psychogiou and R. Gómez-García, "Reflectionless adaptive RF filters: Bandpass, bandstop, and cascade designs," *IEEE Trans. Microw. Theory Techn.*, vol. 65, no. 11, pp. 4593–4605, Nov. 2017.
- [16] D. Psychogiou and R. Gomez-García, "Tunable reflectionless microstrip bandpass filters," in *Proc. IEEE Radio Wireless Symp. (RWS)*, Anaheim, CA, USA, Jan. 2018, pp. 49–51.
- [17] R. Gomez-García, J.-M. Munoz-Ferreras, and D. Psychogiou, "Split-type input-reflectionless multiband filters," *IEEE Microw. Wireless Compon. Lett.*, vol. 28, no. 11, pp. 981–983, Nov. 2018.
- [18] R. Gomez-García, J.-M. Munoz-Ferreras, and D. Psychogiou, "Dual-behavior resonator-based fully reconfigurable input reflectionless bandpass filters," *IEEE Microw. Wireless Compon. Lett.*, vol. 29, no. 1, pp. 35–37, Jan. 2019.
- [19] R. Gomez-García, J.-M. Munoz-Ferreras, and D. Psychogiou, "Symmetrical quasi-reflectionless BSFs," *IEEE Microw. Wireless Compon. Lett.*, vol. 28, no. 4, pp. 302–304, Apr. 2018.
- [20] R. Gomez-García, J.-M. Munoz-Ferreras, and D. Psychogiou, "Symmetrical quasi-absorptive RF bandpass filters," *IEEE Trans. Microw. Theory Techn.*, vol. 67, no. 4, pp. 1472–1482, Apr. 2019.
- [21] X. H. Wu, Y. S. Li, and X. G. Liu, "High-order dual-port quasi-absorptive microstrip coupled line bandpass filters," *IEEE Trans. Microw. Theory Techn.*, vol. 68, no. 4, pp. 1465–1475, Apr. 2020.
- [22] C. Luo *et al.*, "Quasi-reflectionless microstrip bandpass filters using bandstop filter for out-of-band improvement," *IEEE Trans. Circuits Syst. II, Exp. Briefs*, vol. 67, no. 10, pp. 1849–1853, Oct. 2019.
- [23] M. Fan, K. Song, L. Yang, and R. Gómez-García, "Frequency-reconfigurable input-reflectionless bandpass filter and filtering power divider with constant absolute bandwidth," *IEEE Trans. Circuits Syst. II, Exp. Briefs*, vol. 68, no. 7, pp. 2424–2428, Jul. 2021.
- [24] M. Fan, K. Song, L. Yang, and R. Gómez-García, "Frequency-tunable constant-absolute-bandwidth single-/dual-passband filters and diplexers with all-port-reflectionless behavior," *IEEE Trans. Microw. Theory Techn.*, vol. 69, no. 2, pp. 1365–1377, Feb. 2021.
- [25] Z. Cao, X. Bi, and Q. Xu, "Tunable reflectionless filter with independently controllable dual passbands and absorbed harmonic signals," *IEEE Trans. Circuits Syst. II, Exp. Briefs*, early access, May 5, 2021, doi: [10.1109/TCSII.2021.3076499](https://doi.org/10.1109/TCSII.2021.3076499).
- [26] X. Chen, T. Yang, and P.-L. Chi, "Arbitrary-order balanced filter with reflectionless characteristics for both common- and differential-mode signals," *IEEE Microw. Wireless Compon. Lett.*, vol. 31, no. 6, pp. 553–556, Jul. 2021.
- [27] D. M. Pozar, *Microwave Engineering*, 3rd ed. New York, NY, USA: Wiley, 2003.
- [28] W. Feng, X. Ma, Y. Shi, S. Shi, and W. Che, "High-selectivity narrow- and wide-band input-reflectionless bandpass filters with intercoupled dual-behavior resonators," *IEEE Trans. Plasma Sci.*, vol. 48, no. 2, pp. 446–454, Feb. 2020.
- [29] R. Gómez-García, L. Yang, J.-M. Muñoz-Ferreras, and W. Feng, "Lossy signal-interference filters and applications," *IEEE Trans. Microw. Theory Techn.*, vol. 68, no. 2, pp. 516–529, Feb. 2020.



Kai-Da Xu (Senior Member, IEEE) received the B.E. and Ph.D. degrees in electromagnetic field and microwave technology from the University of Electronic Science and Technology of China (UESTC), Chengdu, China, in 2009 and 2015, respectively.

From 2012 to 2014, he was a Visiting Researcher with the Department of Electrical and Computer Engineering, Duke University, Durham, NC, USA, under the financial support from the China Scholarship Council. In 2015, he joined the Department of Electronic Science, Xiamen University, Xiamen, China, as an Assistant Professor. From 2016 to 2017, he was a Postdoctoral Fellow with the State Key Laboratory of Millimeter Waves, City University of Hong Kong, Hong Kong. From 2018 to 2019, he was an Honorary Fellow with the Department of Electrical and Computer Engineering, University of Wisconsin–Madison, Madison, WI, USA. He was successfully selected into the "Youth Talent Support Program" of Xi'an Jiaotong University (XJTU) in May 2019, where he joined the School of Information and Communications Engineering in January 2020. He was awarded a Fellowship from the Japan Society for the Promotion of Science (JSPS) and was the JSPS Fellow with the Department of Communications Engineering, Graduate School of Engineering, Tohoku University from November 2019 to May 2021. He has authored and coauthored over 110 papers in peer-reviewed journals and over 40 papers in conference proceedings. His current research interests include RF/microwave, mm-wave/THz devices, and antenna arrays.

Dr. Xu received the UESTC Outstanding Graduate Awards in 2009 and 2015, respectively. He was a recipient of the National Graduate Student Scholarship in 2012, 2013, and 2014 from the Ministry of Education, China. Since 2017, he has served as an Associate Editor for both of the IEEE *ACCESS* and *Electronics Letters*. He is also an Editorial Board Member of the *AEÜ-International Journal of Electronics and Communications*.



Sen Lu was born in Shandong, China, in 1996. He received the B.Eng. degree in electronic information and engineering from the Northeastern University, Qinhuangdao, China, in 2018. He is currently pursuing the M.Eng. degree with Department of Electronic Science, Xiamen University, Xiamen, China. His research interests include RF and microwave passive components.



Ying-Jiang Guo (Member, IEEE) received the B.E. degree in electronic engineering from Sichuan University, Chengdu, China, in 2008, and the Ph.D. degree in electronic engineering from the University of Electronic Science and Technology in China, Chengdu, in 2018.

From 2011 to 2013, he was with Huawei Technologies Company Ltd., where he was involved in the research of 5G communication prototype design. From 2013 to 2014, he was with Sichuan Normal University, where he was a Lecturer. Since

2018, he has been with Microsystem and Terahertz Research Center, China Academy of Engineering Physics as an Assistant Research Fellow and focuses on the terahertz integrated circuits and communication technologies. He has authored or coauthored over 30 journal and conference papers. He holds over five patents in wireless communication. His research interests include the RF/microwave/mm-wave integrated circuits, THz modules/antennas, and systems in package.



Qiang Chen (Senior Member, IEEE) received the B.E. degree from Xidian University, Xi'an, China, in 1986, and the M.E. and D.E. degrees from Tohoku University, Japan, in 1991 and 1994, respectively.

He is currently the Chair Professor with the Electromagnetic Engineering Laboratory, Department of Communications Engineering, School of Engineering, Tohoku University. His primary research interests include antennas, microwave and millimeter wave, antenna measurement, and computational electromagnetics. He received the Best Paper Award and Zen-ichi Kiyasu Award in 2009 from the Institute of Electronics, Information and Communication Engineers (IEICE). He served as the Chair of IEICE Technical Committee on Photonics-applied Electromagnetic Measurement from 2012 to 2014, IEICE Technical Committee on Wireless Power Transfer from 2016 to 2018, Tokyo Chapter of IEEE Antennas, and Propagation Society from 2017 to 2018. He is currently the Chair of IEICE Technical Committee on Antennas and Propagation. He is an IEICE Fellow.